Principle and Application of the Contactless Load Detection Based on the Amplitude Decay Rate in a Transient Process

Sideng Hu, *Member, IEEE*, Zipeng Liang, Yujie Wang, Jing Zhou, and Xiangning He, *Fellow, IEEE*

***Abstract*—For maximizing the power transfer in an inductive power transfer system, the operating frequency of the system is normally designed to be the same as the resonant frequency of the secondary power pick-up. But the load deviation reflected from secondary side to primary side will result in the frequency mismatch issue. Therefore, the contactless load detection technique is significant to ensure the power transfer efficiency and capacity. The emerging technique taking advantages of the amplitude decay rate in a transient process is promising. The robustness and practicability can get enhanced and the complicated steady circuit model is avoided. However, the accuracy for the small resistance application is still a challenge even with sophisticated compensation algorithms. This paper classified the system detectable region through the root locus method. The transient process in different subregions is excavated mathematically. It is revealed that the variation of the system from the second order to fourth order is the key issue for the detection error in the small load resistance application. The analysis brings out a novel automatic contactless load detection method to extend the detection range. Both simulation and experimental results verified the effectiveness of the proposed theory and detection method.**

***Index Terms*—Contactless load detection, energy injection, inductive power transmission, root locus.**

I. Introduction

THE inductive power transmission (IPT) is becoming popular for the transportation and household appliances due to its clean and convenience [1], [2]. For maximizing the power transfer in an IPT system, the operating frequency of the system is normally designed to be the same as the resonant frequency of the secondary power pick-up. However, one feature of an IPT system is that the deviation of load will reflect from second side to primary side and result in the frequency mismatch issue [3]. As a result, the system efficiency and power transfer capacity will decrease dramatically [4]–[7]. Thus, the load information is essential for the system optimization and control. A few research works on the contactless load identification for the IPT system has been reported. A steady-state load identification method for the IPT system is studied based on switching capacitors [3]. Load identification by detecting the energy dissipation time of self-oscillation circuit is studied in wireless household appliances [8]. A load identification method for the IPT system is proposed based on the least square algorithm [9]. Most of aforementioned methods can achieve good performance through an accurate steady circuit model. However, the high-order and nonlinear characteristics in the IPT steady circuit model are the challenges for their implementations [10]. Recently, a load detection method based on the amplitude decay rate of the voltage or current in the transient process is proposed, aiming to compete with the conventional steady circuit method. This method utilizes the relationship of the system power dissipation and load in the secondary side. It obtained the load information from the voltage or current in primary side. Less parameters are needed and the complicated solution for the high-order model gets avoided. A load detection based on the current decay process is demonstrated in [11] and [12] and it proved to own high accuracy and robustness to the parameter variation. However, there still exist problems for its implementation [5], [11]–[16]: 1) the effective region is narrow. The experimental results show that the accuracy gets deteriorated when the resistor is below $100\,\Omega$; 2) the precondition of its application is not well discussed and demonstrated. Thus, for the error elimination, research works mainly focus on the compensation method like data sampling or processing algorithms; and 3) the offline data processing is often required. An automatic online data processing will make this method more competitive.

In this paper, the principle of the contactless load detection based on the amplitude decay rate in the transient process is researched. Two subregions are classified through the root locus method and the corresponding transient characteristics are excavated mathematically. The deterioration issue for the small load resistance detection in previous research works is revealed. The analysis brings out a novel automatic detection method to extend the detection range. The proposed theory and detection method are verified by simulations and experiments.

Manuscript received June 25, 2016; revised November 25, 2016; accepted January 12, 2017. Date of publication January 23, 2017; date of current version June 23, 2017. This work was supported by the National Natural Science Foundation of China under Grants 51407159 and 51507152. Recommended for publication by Associate Editor S.-C. Tan.

The authors are with the College of Electrical Engineering, Zhejiang University, Hangzhou 310027, China (e-mail: husideng@zju.edu.cn; loavigil@163.com; 1039262849@qq.com; zhoujing_zju@126.com; hxn@zju.edu.cn).

Color versions of one or more of the figures in this paper are available online at http://ieeexplore.ieee.org.

Digital Object Identifier 10.1109/TPEL.2017.2656253

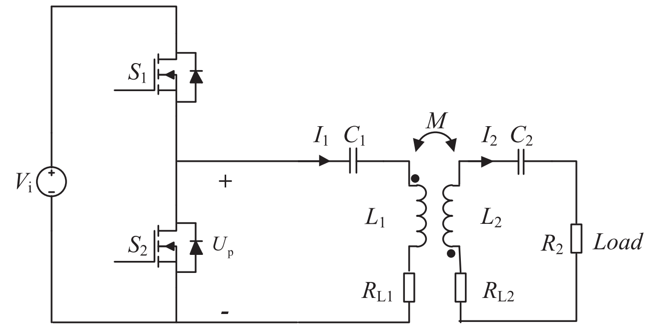

Fig. 1. System diagram.

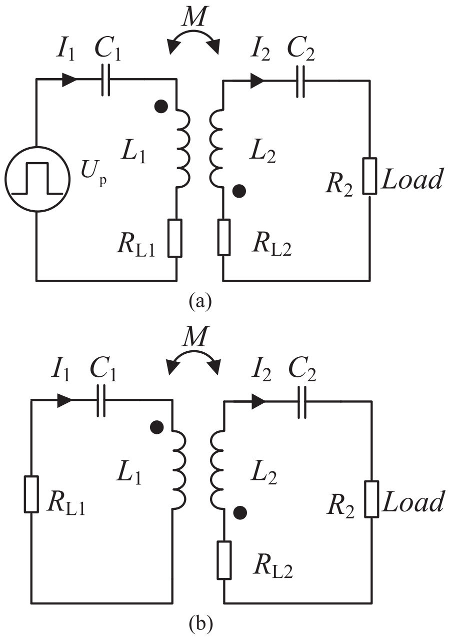

(a)

(b)

Fig. 2. System equivalent circuit in different operation phases. (a) Energy injection phase. (b) Energy dissipation phase.

II. CONTACTLESS LOAD DETECTION BASED ON THE AMPLITUDE DECAY RATE IN THE TRANSIENT PROCESS

A. Basic Principle

The schematic diagram of the contactless load detection based on the amplitude decay rate in the transient process is shown in Fig. 1. There are two phases for the load detection operation [11], as shown in Fig. 2.

In the first phase, a half-bridge converter works in chopping mode. The devices S_1 and S_2 switch in complementary state. Energy is injected through a high frequency square voltage U_p into the coil primary side, as shown in Fig. 2(a). When the first phase finishes, the circuit input voltage gets removed by keeping S_1 OFF and S_2 ON. After that, the system enters the energy dissipation phase, as shown in Fig. 2(b). The energy stored in the circuit gets released and dissipated through the load R_2. The load information can then be obtained by the amplitude decay rate of the inductor voltage or current curve in the transient process.

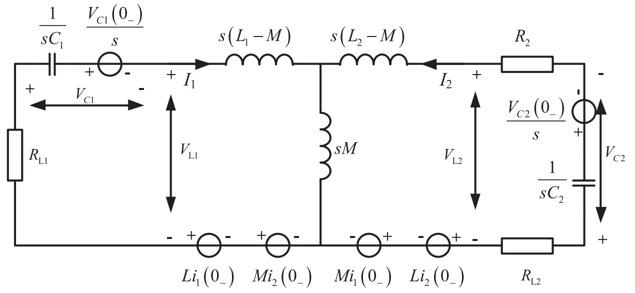

Fig. 3. Complex frequency domain circuit in the energy dissipation phase.

B. Equivalent Circuit and Root Locus of the Contactless Load Detection System

The equivalent circuit in complex region for the circuit in Fig. 2(b) can be expressed as Fig. 3.

The voltage on the inductor L_1 can be derived from Fig. 3 and written as $V_{L1}(\mathrm{s}) = G_{L1} \cdot N(\mathrm{s})/F(\mathrm{s})$, where G_{L1}, $N(\mathrm{s})$, and $F(\mathrm{s})$ represents the voltage amplitude on frequency domain, the numerator equation, and the denominator equation, respectively. The characteristic equation $F(\mathrm{s}) = 0$ is as follows:

$$\left(s^2 + \frac{R_{L1}}{L_1}s + \frac{1}{L_1C_1}\right) \times \left(s^2 + \frac{R_2 + R_{L2}}{L_2}s + \frac{1}{L_2C_2}\right) - k_T^2 s^4 = 0 \quad (1)$$

where R_{L1}, L_1, and C_1 mean the resistor, inductor, and capacitor in the primary side, respectively, and R_{L2}, L_2, and C_2 mean the resistor, inductor, and capacitor in the secondary side, respectively. R_2 means the load. *M* means the mutual inductance of the coils. k_T means the coupling factor of the inductors and $k2T = M^2/L_1L_2$. The roots of (1): s_n $(n = 1, 2, 3, 4)$ correspond to four poles of the system. The system root locus equation for (1) can be written as follows:

$$G(s) + 1 = 0$$

$$G(s) = \frac{R_2 \cdot \frac{1}{L_2} s \left(s^2 + \frac{R_{L1}}{L_1}s + \frac{1}{L_1C_1}\right)}{\left(s^2 + \frac{R_{L2}}{L_2}s + \frac{1}{L_2C_2}\right)\left(s^2 + \frac{R_{L1}}{L_1}s + \frac{1}{L_1C_1}\right) - k_T^2 s^4}. \quad (2)$$

Assuming $L_1 = L_2 = L$, $C_1 = C_2 = C$, the 3-D locus of s_n with R_2 as the *Z*-axis is shown in Fig. 4(a). Corresponding 2-D root locus curves are shown in Fig. 4(b). In Fig. 4(b), s_1 and s_3 forms a pair of complex-conjugate poles. According to the existence conditions for the dominant poles [17], the dominant poles should be significantly closer to imaginary axis than other poles like $|\alpha_2|, |\alpha_4| \geq \lambda|\alpha_1|, \lambda \geq 5$. Thus, define the critical value of load resistor corresponding to the dominant poles existence condition as R^*. Then, Fig. 4 can be divided into two subregions: *H* region $(0 < R_2 < R^*)$ and *K* region $(R^* < R_2 < R_{\max})$. The root locus in *H* and *K* regions is expressed in Table I.

In Fig. 3, $R_2 = R^*$ can be viewed as a plane named Σ. The region above Σ means the *K* region and the one below Σ is the

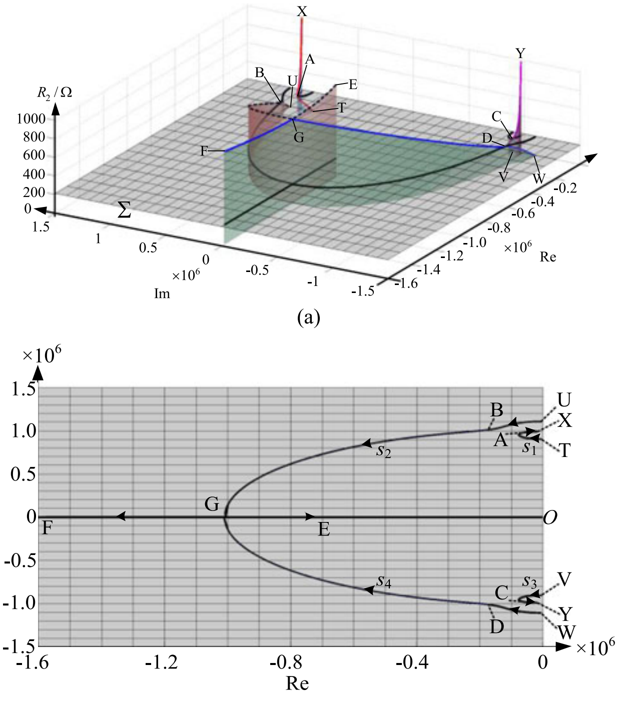

(a)

(b)

Fig. 4. System root locus plot: (a) three dimension and (b) two dimension.

TABLE I
ROOT LOCUS IN *H* AND *K* REGIONS

Poles	Expression	Locus	*H* region	*K* region
s_1	$\alpha_1 + j\omega_1$	TX	TA	XA
s_2	$\alpha_2 + j\omega_2$	UGE	UB	BGE
s_3	$\alpha_1 - j\omega_1$	VY	VC	CY
s_4	$\alpha_4 + j\omega_4$	WGF	WD	DGE

H region. In the *K* region, the existence condition for the dominant poles is satisfied. There exists a pair of dominant poles s_1 and s_3. In the *H* region, no dominant pole exists.

III. CHARACTERISTICS OF POLES, TRANSIENT PROCESS, AND DETECTION METHOD IN SUBREGIONS *H* AND *K*

The characteristics of poles in subregions *H* and *K* are studied in this section to illustrate the corresponding transient process. The real parts of the poles affect the decay rate while the imaginary parts determine the oscillation frequency. The curves of the real parts (α_1, α_2 and α_3) can be found by the projection of Fig. 3 on real axis, as shown in Fig. 5. The line β in Fig. 5 represents $\lambda\alpha_1$. The curves of the imaginary part (ω_1, ω_2, and ω_3) are shown in Fig. 6 by the projection on the imaginary axis. Then, the characteristics of the poles in *K* and *H* regions will be discussed from the real and imaginary parts in following sections.

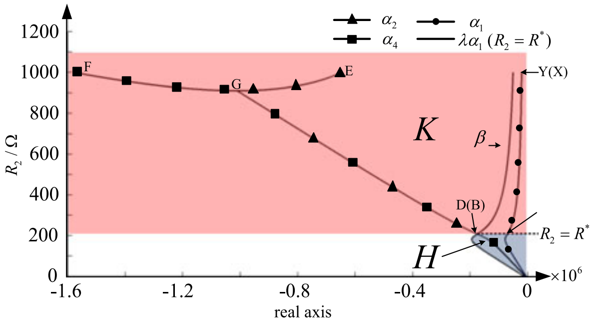

Fig. 5. Relationship between the real part and R_2.

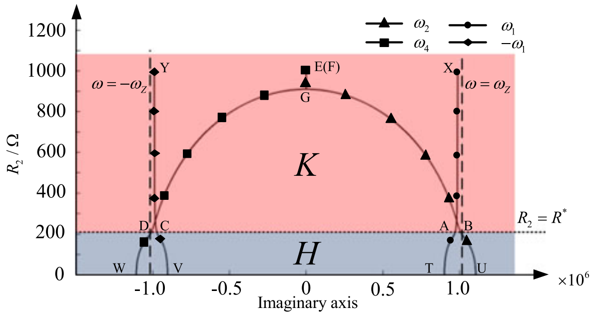

Fig. 6. Relationship between the imaginary part and R_2.

A. *Poles Characteristics in K Region*

The real parts of the poles in *K* region satisfy

$$\alpha_2|, |\alpha_4| \geq \lambda|\alpha_1| \text{ and } \lambda \geq 5. \tag{3}$$

Thus, the system can be viewed as a second-order system and the transient process is dominated by s_1 and s_3.This is the poles real part characteristic in *K* region.

According to the root locus theory, s_1 and s_3 converge to the zeroes s_z of *G*(s) in (2) as follows:

$$\lim_{R_2 \to \infty} s_{1,3} = s_Z = -\frac{R_{L1}}{2L} \pm j\sqrt{\omega_0^2 - \left(\frac{R_{L1}}{2L}\right)^2} \tag{4}$$

where ω_0 the oscillation frequency and $\omega_0 = \sqrt{1/LC}$, and ω_z means the absolute value of the imaginary part in s_z

$$\omega_Z = \sqrt{\omega_0^2 - \left(\frac{R_{L1}}{2L}\right)^2}$$

when $\frac{R_{L1}}{2L} \ll \omega_0$, we get

$$\omega_1 \approx \omega_0 \approx \omega_Z. \tag{5}$$

Equation (5) means the imaginary part of s_1 and s_3 are close to ω_0. This is the poles imaginary part characteristic in *K* region.

As shown by the curves in Figs. 5 and 6, the amplitude of the real part and imaginary part in *K* region satisfy

$$\left|\frac{\alpha_1}{\omega_1}\right| \approx 0.1 \ll 1. \tag{6}$$

Equation (6) implies that the absolute value of real part is much smaller than the imaginary part for the dominant poles. This is named as the poles combination characteristic.

B. Poles Characteristics in H Region

As the R_2 decreases, the poles move from *K* region to *H* region. As shown in Fig. 6, all the poles will locate in the right side of β

$$\lambda|\alpha_1| > |\alpha_2| = |\alpha_4| \approx |\alpha_1|. \tag{7}$$

The system performs as a fourth-order system. As no dominant pole exists in *H* region, the responses of the poles s_2 and s_4 cannot be neglected. This is the poles real part characteristic in *H* region.

As shown in Fig. 6, the relationship of the imaginary part can be expressed as follows:

$$\omega_1 \approx \omega_2 = -\omega_4. \tag{8}$$

It means that the oscillation frequencies of the poles are close to each other. This is the imaginary part characteristic in *H* region.

Based on the aforementioned analysis, it can be concluded that there exists a pair of dominant poles in *K* region and the imaginary parts of them are close to ω_0. The transient process can be viewed as a second-order system response. In *H* region, by contrast, no dominant poles exist so the transient process is a fourth-order system response. In following sections, the detailed transient processes in *K* and *H* regions are explained based on aforementioned characteristics.

C. Transient Process in K Region and Detection Method

Based on the imaginary part characteristic and combination characteristic in *K* region, it can be found that

$$\begin{aligned} s_{1,3} &= \alpha_1 \pm j\omega_1 \\ &\approx \pm j\omega_0. \end{aligned} \tag{9}$$

Then, the characteristic equation (1) can then be simplified as (10) in *K* region. The dominant poles s_1 and s_3 shape the transient process like the underdamped second-order linear system as Fig. 7. V_{L0} in Fig. 7 means the initial voltage in L_1 in the energy dissipation phase

$$s^2 + \frac{R_{L1} + R_x}{L} s + \omega_0^2 = 0 \text{ where } R_x = \frac{\omega_0^2 M^2}{R_2 + R_{L2}}. \tag{10}$$

According to Vieta's formulas from (10), α_1 can be derived as follows:

$$\alpha_1 = -\frac{R_{L1} + \omega_0^2 M^2/(R_2 + R_{L2})}{2L}. \tag{11}$$

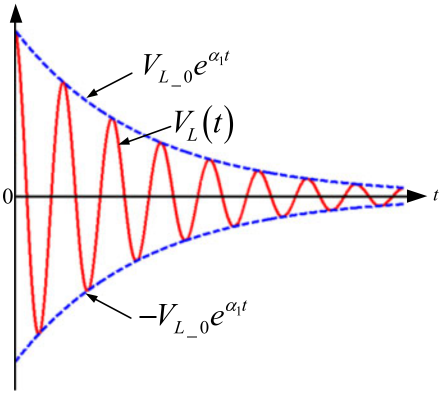

Fig. 7. Curve of the inductor voltage in *K* region.

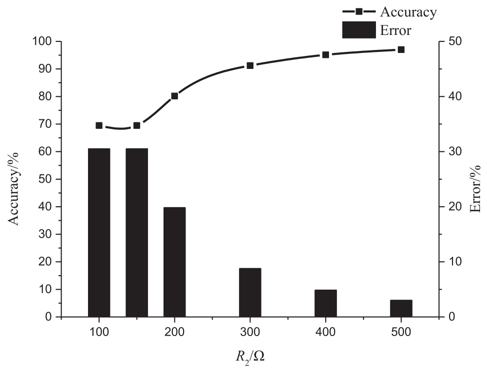

Fig. 8. Detection accuracy and error in *K* region.

TABLE II
SIMULATION AND EXPERIMENTAL PARAMETERS

Parameter name	Value	Parameter name	Value
Peak input voltage U_{in}/V	5.0	Switching frequency f_{sw}/kHz	156
R_{L1}/Ω	10.0	$R_{p1}/\text{k}\Omega$	4.0
R_{L2}/Ω	15.5	$R_{p2}/\text{k}\Omega$	10
$C_2, C_1/\text{nF}$	2.2	$R_{\text{ed}}/\text{k}\Omega$	1.0
$L_1/\mu\text{H}$	465	C_{ed}/nF	10
$L_2/\mu\text{H}$	474	$R_{\text{lpf}}/\text{k}\Omega$	1.1
Coupling factor for L_1 $L_{2:}$ k_T	0.20	C_{lpf}/nF	2.2

Equation (11) is the same with the load detection model in [12]. Thus, the methods in [12] can be cataloged into *K* region and (3) is its precondition. According to the derivation in the Appendix, we get R_2 from (3) as follows:

$$\begin{aligned} R_2 \geq &\left(2.5 - 3\,k_T^2\right) R_{L1} - R_{L2} \\ &+ \sqrt{\left(2.5 - 3k_T^2\right)^2 R_{L1}^2 + \frac{6L}{C} k_T^2 \left(1 - k_T^2\right)}. \end{aligned} \tag{12}$$

Equation (12) means the lower bond of R_2 for the *K* region. As R_2 decreases, the system will leave *K* region and enter *H* region. Thereby, (3) and (10) is not satisfied. Above implies that the detection error in *H* region is inevitable. This is consistent with the experimental phenomena in [12], where the accuracy deteriorated dramatically for the small R_2. The theoretical error e_k with R_2 is demonstrated in Fig. 8 with the parameters listed in Table II.

As R_2 decreases in Fig. 8, the system leaves the *K* region gradually. The results show that the detection error is relatively small when the $R_2 > 300\ \Omega$. When $R_2 < 300\ \Omega$, the detection error increased significantly.

D. Transient Process in H Region and Corresponding Detection Method

Since the method in [12] is suitable for *K* region, a novel method for the *H* region detection is studied in this section. As the responses of s_2 and s_4 cannot be neglected, V_{L1} in time domain should be rewritten as follows:

$$\begin{aligned} V_{L1} &= A_1 e^{\alpha_1 t}\sin(\omega_1 t + \varphi_1) + A_2 e^{\alpha_2 t}\sin(\omega_2 t + \varphi_2) \\ &= \left(A_1 e^{\alpha_1 t} + A_2 e^{\alpha_2 t}\right)\cos\left(\frac{\omega_1 - \omega_2}{2}t + \frac{\varphi_1 - \varphi_2}{2}\right) \\ &\quad \cdot \sin\left(\frac{\omega_1 + \omega_2}{2}t + \frac{\varphi_1 + \varphi_2}{2}\right) + \left(A_1 e^{\alpha_1 t} - A_2 e^{\alpha_2 t}\right) \\ &\quad \cdot \sin\left(\frac{\omega_1 - \omega_2}{2}t + \frac{\varphi_1 - \varphi_2}{2}\right) \\ &\quad \times \cos\left(\frac{\omega_1 + \omega_2}{2}t + \frac{\varphi_1 + \varphi_2}{2}\right). \end{aligned} \tag{13}$$

According to the Laplace theorem, we can get

$$\begin{aligned} A_1 &= 2G_{L1}\left|\frac{(s_1 - z_1)(s_1 - z_2)(s_1 - z_3)}{(s_1 - s_2)(s_1 - s_3)(s_1 - s_4)}\right| \\ &= 2G_{L1}\frac{|s_1 - z_1|\cdot|s_1 - z_2|\cdot|s_1 - z_3|}{|s_1 - s_2|\cdot|s_1 - s_3|\cdot|s_1 - s_4|} \\ A_2 &= 2G_{L1}\left|\frac{(s_2 - z_1)(s_2 - z_2)(s_2 - z_3)}{(s_2 - s_1)(s_2 - s_3)(s_2 - s_4)}\right| \\ &= 2G_{L1}\frac{|s_2 - z_1|\cdot|s_2 - z_2|\cdot|s_2 - z_3|}{|s_1 - s_2|\cdot|s_2 - s_3|\cdot|s_2 - s_4|} \\ \frac{A_1}{A_2} &= \frac{|s_1 - z_1|}{|s_2 - z_1|}\cdot\frac{|s_1 - z_2|}{|s_2 - z_2|}\cdot\frac{|s_1 - z_3|}{|s_2 - z_3|}\cdot\frac{|s_2 - s_3|}{|s_1 - s_3|}\cdot\frac{|s_2 - s_4|}{|s_1 - s_4|} \end{aligned}$$

where z_n $(n = 1, 2, 3)$ represents the zeroes in $V_{L1}(\mathrm{s})$. According to the poles characteristics as (7) and (8), we can get

$$A_1 \approx A_2. \tag{14}$$

Therefore, (15) can be obtained from (7), (13), and (14). The corresponding inductor voltage is shown in Fig. 9

$$\begin{aligned} V_{L1} &\approx (A_1 + A_2)\,e^{\frac{\alpha_1 + \alpha_2}{2}t}\cos\left(\frac{\omega_1 - \omega_2}{2}t + \frac{\varphi_1 - \varphi_2}{2}\right) \\ &\quad \cdot \sin\left(\frac{\omega_1 + \omega_2}{2}t + \frac{\varphi_1 + \varphi_2}{2}\right) \\ &= (A_1 + A_2)\,e^{\alpha_h t}\cos\left(\omega_d t + \frac{\varphi_1 - \varphi_2}{2}\right) \\ &\quad \cdot \sin\left(\omega_c t + \frac{\varphi_1 + \varphi_2}{2}\right) \end{aligned} \tag{15}$$

where $\omega_\mathrm{d} = \frac{\omega_1 - \omega_2}{2}$ and $\omega_\mathrm{c} = \frac{\omega_1 + \omega_2}{2}$

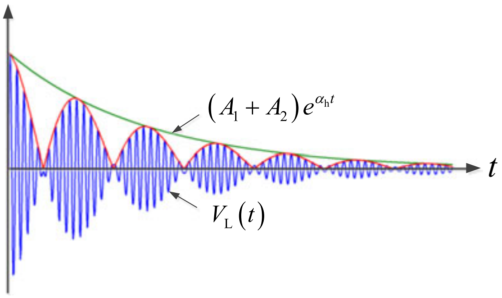

Fig. 9. Inductor voltage curve for *H* region.

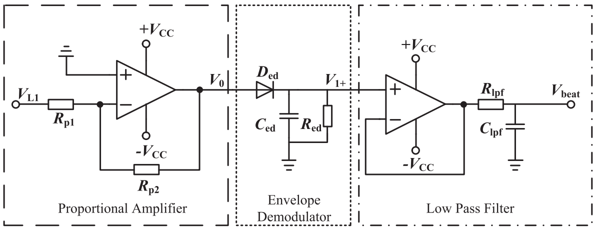

Fig. 10. Implementation of the load detection circuits.

According to the imaginary part characteristic as (8), it is easy to get $\omega_d << \omega_c$. Fig. 9 shows that a typical beat phenomenon for the fourth-order system occurs with exponential decaying beat amplitude. Define the amplitude decay rate in *H* region α_h as follows:

$$\alpha_h = (\alpha_1 + \alpha_2)/2. \tag{16}$$

According to Vieta's formulas, the relationship of R_2 and α_h can be derived from (1) as follows:

$$\sum_{i=1}^{4} s_i = 2(\alpha_1 + \alpha_2) = -\frac{R_{L1} + R_2 + R_{L2}}{L\left(1 - {k_T}^2\right)} \tag{17}$$

$$\alpha_h = (\alpha_1 + \alpha_2)/2 = -\frac{R_{L1} + R_2 + R_{L2}}{4L(1 - {k_T}^2)} \tag{18}$$

$$R_2 = -4(1 - {k_T}^2)L\alpha_h - R_{L1} - R_{L2}. \tag{19}$$

From (19), R_2 is a monotonic function of α_h with a linearity of –$4(1 - k_T^2)L$. Then, the load value can be obtained by measuring α_h. For the steady circuit method [3], not only the value of the inductance, resistance, and peak current but also the value of frequency, input voltage, and resonant capacitor are needed for the resistor detection. The solution of a high-order system is also a challenge. However, the amplitude decay rate method based on (19) takes advantage of the relationship between the power decay rate and load. According to (19), only the value of the inductance, resistance, and peak current are needed. Thus, the system is more robust to the parameter deviation.

E. Implementation of the Proposed Method for H Region

The measurement of α_h is discussed in this section from the hardware circuits and software algorithm. The signal sampling circuit is designed to extract the positive beat envelope of V_L, as demonstrated in Fig. 10. It is formed by a proportional

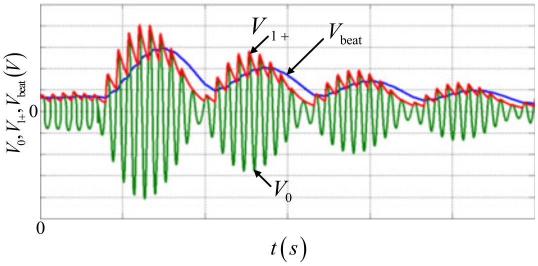

Fig. 11. Voltage curves in the test procedures.

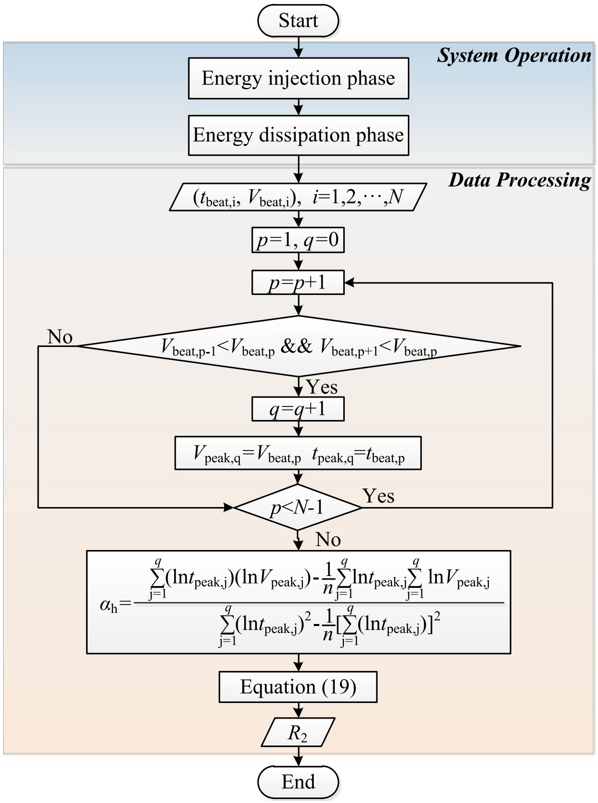

Fig. 12. Detection flowchart of the proposed method.

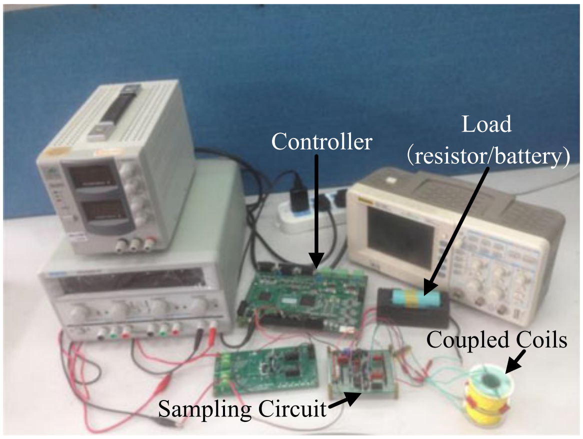

Fig. 13. Experimental platform.

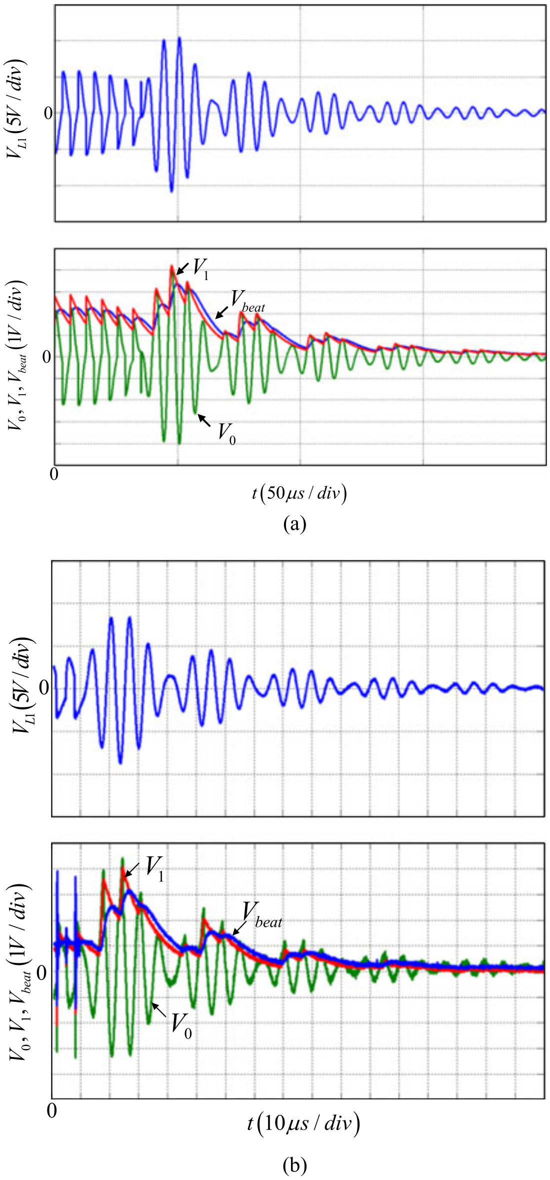

Fig. 14. Load detection and signal processing: (a) simulation and (b) experiment.

TABLE III
VERIFICATION FOR THE TRANSIENT PROCESS ANALYSIS IN *H* REGION

	Theoretical value	Simulation value	Experimental value
V_L decay rate	–23 600	–23 543	–23 599
V_{beat} decay rate	–23 600	–23 602	–23 582
Load resistor/Ω	1.0	1.01	0.97

amplifier, an envelope demodulator, and a low-pass filter. The corresponding output signal waveforms are shown in Fig. 11.

The proportional amplifier makes the ration between V_0 and V_{L1} equal to $-R_{p2}/R_{p1}$. The envelope demodulator extracts the envelope of the peak value of V_0. The envelope curve is defined as V_{1+} and is related with the value of $R_{\mathrm{ed}}C_{\mathrm{ed}}$, which should

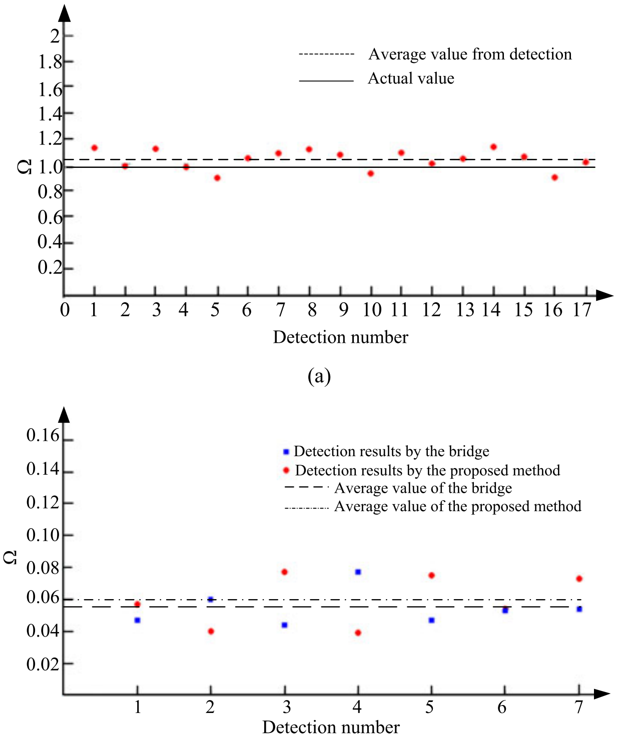

(a)

(b)

Fig. 15. Comparison of the experimental results: (a) load resistance and (b) battery internal resistance.

satisfy (20) based on the derivation in the Appendix

$$R_{\mathrm{ed}}C_{\mathrm{ed}} \leq \frac{4L(1-{k_T}^2)}{R_{L1}+R^*+R_{L2}}. \tag{20}$$

The low-pass filter is designed to reduce the high frequency ripple in V_{1+} and output the filtered beat envelope V_{beat} for analog-to-digital converter devices. The bandwidth of the filter should satisfy (21) according to (14)

$$\omega_d \leq \mathrm{BW} = \frac{1}{R_{\mathrm{lpf}}C_{\mathrm{lpf}}} \leq \omega_c. \tag{21}$$

Finally, the overall operation is demonstrated as Fig. 12 and separated into two procedures: system operation and data processing. Both of these procedures are carried out by the controller automatically.

During the data processing procedure, N sampled data of V_{beat} and corresponding time are acquired in the energy dissipation phase. After that, α_h is calculated and the load value R_2 is detected based on (19).

IV. SIMULATION AND EXPERIMENTAL RESULTS

In this section, the proposed detection method for *H* region will be verified by the simulations and experiments. The platform and the parameters are demonstrated in Fig. 13 and Table II. The test value of R_2 equals to 1 Ω.

The simulation and experimental waveforms are shown in Fig. 14. The results are shown in Table III.

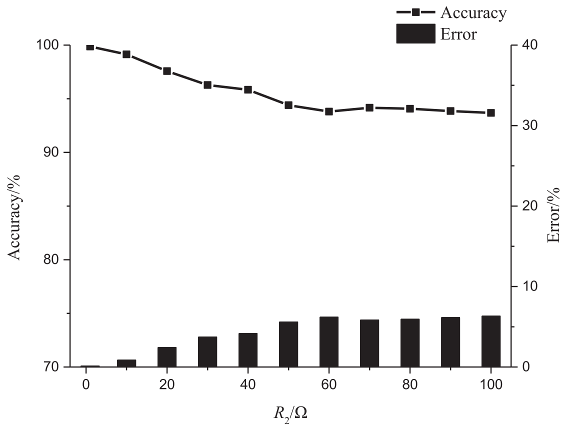

Fig. 16. Detection accuracy and error by the proposed method in *H* region.

The theoretical value of decay rate is calculated based on (18). It can be found that the simulation and experimental results are close to the theoretical ones. An error analysis is carried out through multiple detections and the results are shown in Fig. 15.

Fig. 15(a) shows that the detection results reach good consistency. The average value of the detection results is 1.03 Ω and the standard deviation is 0.08 Ω. Then, the method is tested by detecting the internal resistor of a battery. The test results are shown in Fig. 15(b) and the average value is 0.59 Ω. The standard deviation is 0.02 Ω. The average test value by a bridge is 0.55 Ω and the standard deviation is 0.02 Ω. The results by the proposed contactless load detection method are similar to the bridge results. That implies the proposed method can be applied to the battery safety application based on the internal resistor.

Finally, the detections with other load values below 100 Ω are demonstrated in Fig. 16.

Compared with the results in Fig. 8, the detection accuracy in Fig. 16 gets improved around 100 Ω. It can be found that a better accuracy can be achieved with smaller load resistor.

This is consistent with the poles characteristics analysis in *H* region, because (7) and (8) are better satisfied with a smaller load resistor.

V. CONCLUSION

In this paper, the principle of the contactless load detection based on the amplitude decay rate in the transient process is researched. The characteristics of the detectable region are studied through the system root locus method. The results show that, as the load resistor value decreases, the system transient process will transfer from a second-order type into a four order type. This is the key issue for the deterioration issue in the conventional method with small resistance application. Based on that a detection method for the small load resistor region is proposed. Both simulation and experimental results verified the effectiveness. Meanwhile, the capability to monitor the internal resistor in the battery package is demonstrated. The method can also be applied to other topologies for the contactless load detection.

APPENDIX

A. Lower Bond of the Detection Method for K Region

The real part of dominant poles in the *K* region is shown as (11) in Section III and Vieta's formulas for (1) is demonstrated as follows:

$$\sum_{i=1}^{4} s_i = 2\left(\alpha_1 + \alpha_2\right) = -\frac{R_{L1} + R^* + R_{L2}}{L\left(1 - {k_T}^2\right)}. \tag{22}$$

Then, the inequality for R_2 can be obtained based on (3), (11), and (22)

$$R_2 \geq \left(2.5 - 3\,k_T^2\right) R_{L1} - R_{L2} + \sqrt{\left(2.5 - 3k_T^2\right)^2 R_{L1}^2 + \frac{6L}{C} k_T^2 \left(1 - k_T^2\right)}. \tag{23}$$

B. Parameter Design for the Envelope Demodulator

The envelope demodulator aims to extract the envelope of V_0. When the diode $D_{\rm ed}$ is blocked, the decay ratio of V_{1+} is equal to $-1/R_{\rm ed}C_{\rm ed}$. To acquire the peak value of the beats, decay ratio of V_{1+} should be higher than the decay ratio of V_0, which is defined as α_h in (16). Then, we get

$$-\frac{1}{R_{\rm ed}C_{\rm ed}} \leq \alpha_h \tag{24}$$

$$R_{\rm ed}C_{\rm ed} \leq \frac{1}{-\alpha_h} = \frac{4L(1 - {k_T}^2)}{R_{L1} + R_2 + R_{L2}}. \tag{25}$$

In order to cover the *H* region, we can substitute R^* into (25)

$$R_{\rm ed}C_{\rm ed} \leq \frac{4L(1 - {k_T}^2)}{R_{L1} + R^* + R_{L2}} \tag{26}$$

where R^* is the upper region of *H* region, as discussed in Section II-B.

REFERENCES

[1] W. Zhang, S. Wong, C. K. Tse, and Q. Chen, "Analysis and comparison of secondary series- and parallel-compensated inductive power transfer systems operating for optimal efficiency and load-independent voltage-transfer ratio," *IEEE Trans. Power Electron.*, vol. 29, no. 6, pp. 2979–2990, Jun. 2014.

[2] P. Raval, D. Kacprzak, and A. P. Hu, "Analysis of flux leakage of a 3-D inductive power transfer system," *IEEE J. Emerg. Sel. Topics Power Electron.*, vol. 3, no. 1, pp. 205–214, Mar. 2015.

[3] Y. Su, H. Zhang, Z. Wang, A. P. Hu, L. Chen, and Y. Sun, "Steady-state load identification method of inductive power transfer system based on switching capacitors," *IEEE Trans. Power Electron.*, vol. 30, no. 11, pp. 6349–6355, Nov. 2015.

[4] J. Yin, D. Lin, C. Lee, and S. Y. R. Hui, "A systematic approach for load monitoring and power control in wireless power transfer systems without any direct output measurement," *IEEE Trans. Power Electron.*, vol. 30, no. 3, pp. 1657–1667, Mar. 2015.

[5] C. S. Wang, G. A. Covic, and O. H. Stielau, "Power transfer capability and bifurcation phenomena of loosely coupled inductive power transfer systems," *IEEE Trans. Ind. Electron.*, vol. 51, no. 1, pp. 148–157, Feb. 2004.

[6] A. Trigui, S. Hached, F. Mounaim, A. C. Ammari, and M. Sawan, "Inductive power transfer system with self-calibrated primary resonant frequency," *IEEE Trans. Power Electron.*, vol. 30, no. 11, pp. 6078–6087, Nov. 2015.

[7] J. Zhou, Y. Gao, X. Huang, S. Hu, and Y. Fang, "Voltage transfer ratio analysis for multi-receiver resonant power transfer systems," *IET Power Electron.*, vol. 9, no. 15, pp. 2795–2802, Dec. 2016.

[8] X. Dai, Y. Sun, C. S. Tang, Z. H. Wang, Y. G. Su, and Y. L. Li, "Dynamic parameters identification method for inductively coupled power transfer system," in *Proc. IEEE Int. Conf. Sustain. Energy Technol.*, 2010, pp. 1–5.

[9] Y. Su, L. Chen, Z. Wang, A. P. Hu, and X. Dai, "A load identification method for inductive power transfer system based on the least square algorithm," *Trans. China Electrotech. Soc.*, vol. 30, no. 5, pp. 9–14, Mar. 2015.

[10] A. P. Sample, D. A. Meyer, and J. R. Smith, "Analysis, experimental results, and range adaptation of magnetically coupled resonators for wireless power transfer," *IEEE Trans. Ind. Electron.*, vol. 58, no. 2, pp. 544–554, Feb. 2011.

[11] C. Zhao, J. Du, J. Wu, X. He, and M. Yan, "Contactless measurement of temperature based on transient wireless energy transmission," in *Proc. IEEE Appl. Power Electron. Conf. Expo.*, Mar. 2013, pp. 3107–3111.

[12] Z. Wang, Y. Li, Y. Sun, C. Tang, and X. Lv, "Load detection model of voltage-fed inductive power transfer system," *IEEE Trans. Power Electron.*, vol. 28, no. 11, pp. 5233–5243, Nov. 2013.

[13] X. Lv, L. Zhang, and D. Zou, "An approach for detecting illegal load in wireless power transfer system," *Appl. Mech. Mater.*, vol. 599–601, pp. 798–801, 2014.

[14] X. Dai, Y. Sun, C. Tang, Z. Wang, Y. Su, and Y. Li, "Dynamic parameters identification method for inductively coupled power transfer system," in *Proc. IEEE Int. Conf. Sustain. Energy Technol.*, 2010, pp. 1–5.

[15] Z. Wang, X. Lv, Y. Sun, X. Dai, and Y. Li, "A simple approach for load identification in current-fed inductive power transfer system," in *Proc. IEEE Int. Conf. Power Syst. Technol.*, Nov. 2012, pp. 1–5.

[16] J. Yin, D. Lin, C. K. Lee, and S. Y. R. Hui, "Load monitoring and output power control of a wireless power transfer system without any wireless communication feedback," in *Proc. IEEE Energy Convers. Congr. Expo.*, Sep. 2013, pp. 4934–4939.

[17] R. C. Dorf and R. H. Bishop, *Modern Control System*, 10th ed. Upper Saddle River, NJ, USA: Pearson Education, Inc., 2005.

Sideng Hu (M'14) was born in China, in 1984. He received the Ph.D. degree in power electronics from Tsinghua University, Beijing, China, in 2011.

From August 2011 to August 2013, he was a Postdoctoral Researcher with the University of Michigan, Dearborn, MI, USA. Since September 2013, he has been with the College of Electrical Engineering, Zhejiang University, Hangzhou, China. His research interests include high-frequency dc/dc converters, and vehicle electrification.

Zipeng Liang was born in China, in 1992. He received the bachelor's degree in electronic engineering from Zhejiang University, Hangzhou, China, in 2015, where he has been working toward the Ph.D. degree in the College of Electrical Engineering since July 2015.

His research interests include power converters, renewable energy, and vehicle electrification.

Yujie Wang was born in China, in 1994. She received the B.E. degree in electronic engineering from Nanjing University of Technology, Nanjing, China, in 2015. She joined the College of Electrical Engineering, Zhejiang University, Hangzhou, China, in September 2016, where she is currently working toward the M.E. degree.

Her research interests are in advanced control for power electronics and energy storages.

Jing Zhou received the bachelor's degree from Xi'an Jiaotong University, Xi'an, China, in 2011, and the Ph.D. degree from Imperial College London, London, U.K., in 2014, all in mechanical engineering.

She continued her research as a Postdoctoral Researcher at Zhejiang University, Hangzhou, China. Her research mainly focuses on multifield coupled analysis and wireless power transfer.

Xiangning He (M'95–SM'96–F'10) received the B.Sc. and M.Sc. degrees from Nanjing University of Aeronautical and Astronautical, Nanjing, China, in 1982 and 1985, respectively, and the Ph.D. degree from Zhejiang University, Hangzhou, China, in 1989, all in power electronics.

He is currently a Professor in the College of Electrical Engineering, Zhejiang University, Hangzhou, China.

Dr. He has been appointed as an IEEE Distinguished Lecturer by the IEEE Power Electronics Society in 2011. He is also a Fellow of the Institution of Engineering and Technology (formerly IEE), U.K.